A modal approach for shape defect measurement based on global stereocorrelation

David Etievant, Yann Quinsat, François Thiebaut, François Hild

A modal approach for shape defect measurement based on global stereocorrelation

David Etievant[a], Yann Quinsat[a], François Thiebaut[a], François Hild[b]

[a] LURPA / ENS Paris Saclay / Université Paris-Saclay 61 Avenue du Président Wilson, 94235 Cachan Cedex, France
[b] Laboratoire de Mécanique et Technologie (LMT) / ENS Paris Saclay / CNRS-UMR 8535 / Université Paris-Saclay 61 Avenue du Président Wilson, 94235 Cachan Cedex, France

Abstract

The metrology of mechanical parts using non-contact systems often requires complex post-processing operations to evaluate shape defects of the studied surface. For large parts, the geometric complexity combined with the amount of acquired data make such treatments long and tedious. To overcome this challenge, a shape defect measurement system based on global stereocorrelation is developed. This approach integrates a self-calibration step using the CAD model of the studied part that allows the measurement results to be directly expressed in the numerically defined frame of the part. The defects will be measured in a predefined modal basis, thereby introducing registrations with a limited number of degrees of freedom and allowing for easier analyses of the measured defects.

Keywords: Inspection, Modal basis, Shape defect, Stereo-DIC

1. Introduction

Manufactured mechanical parts have shapes that differ from their nominal description, which is defined numerically (*e.g.,* via CAD and/or FE models). Depending on the wavelength of the geometric deviations, a classification is performed to separate defect typologies into position, orientation, shape, undulation and roughness [1]. These differences are evaluated from the comparison between the surface acquisition and its nominal definition. Current acquisition systems typically provide point clouds, which require *a posteriori* processing to keep only the significant deviations from the studied defect [2]. In this context, optical methods are increasingly used due to the good compromise between acquisition speed and measurement uncertainties. This is especially true for the metrology of large parts [3], where the improvements of both CCD/CMOS sensors and computation schemes allowed for the implementation of methods that only existed as concepts before [4].

However, if the user is interested in the measurement and quantification of shape defects, one of the major limitations to the use of optical systems concerns post-processing steps of the measured data. The

---

latter ones acquired by optical means are often heterogeneous, noisy and may have scanning gaps due to the complexity of the surface of interest [5]. This is why the measurements may become complex and the defect quantification a real challenge. Another issue is related to the matching of measurements with the theoretical surface definition. The most common methods rely on Iterative Closest Point (ICP) algorithms [6, 7] and may induce some additional errors in the determination of deviations [8].

The defects in position, orientation and shape of an object entity will be described with a selected library. For elementary or parametric surfaces (*e.g.,* Bézier patches), these descriptions are generally based on trigonometric functions or polynomials. For example, Huang et al. [9] used Discrete Cosine Transforms to express the shape defect of a workpiece. For optical components, the library was usually decomposed via Zernike polynomials considering that each elementary defect represents a characteristic optical distortion [10]. Ganti et al. [11] selected the so-called Weierstrass-Mandelbrot functions. These different approaches enable the shape defects of a workpiece to be described with few parameters. However they are mainly limited to elementary surfaces.

To extend the representation of shape defects to complex surfaces, Franciosa et al. [12] proposed to use mesh morphing techniques based on computer graphics tools to quantify shape deviations. This technique enables a wide range of shape defects to be represented. However, its characterization is highly dependent on the different parameters (*e.g.,* distance from hull and shape functions). Samper et al. [13] suggested to express the shape defects using a modal decomposition based on free vibrational modes. The amplitude of higher modal wavelengths usually decreased (as the frequency increased). Thus the entire basis is generally not needed to model shape defects. One can obtain a good description of shape defects with a restricted number of modes, thereby reducing the number of degrees of freedom of the defect library.

It is worth noting that the modal approach is the object of standards [14, 15] for the analysis and characterization of shape defects on elementary features (*e.g.,* planes, cylinders, cones and circles). Even though these documents only deal with simple geometries, the description of shape defects by eigenmodes can be applied for any geometric complexity of the surface of interest, and any dimension by using finite element solutions. This approach was used, for example, to evaluate defects of large flexible parts [16].

To determine and characterize shape defects of mechanical parts, the studied surface should first be measured. As they can be potentially flexible and large, it is necessary to use non-contact techniques for which the spatial resolution can easily be adapted. This is the case of image correlation techniques. Even though mostly used for displacement measurements, stereocorrelation techniques can be utilized for shape measurements [17, 18]. The position in the 3D space of multiple points are calculated using projection matrices that are estimated during the calibration phase. Each "point" corresponds to the center of a small interrogation window that is registered between images acquired by two cameras and are reconstructed by triangulation. This approach provides a large amount of points, which help for analyzing complex geometries (*e.g.,* the topography of a tunnel portion [19]). However, the output is a point cloud, which involves a complex

2

and time-consuming post-processing step. A second approach, similar to global approaches adopted in 2D-DIC (2D Digital Image Correlation) [20, 21] consists in mathematically modeling the studied surface (by NURBS [22, 23] or finite element meshes [24, 25]), and to determine the displacement field to apply to minimize the correlation residual computed over the entire region of interest. This technique provides a dense description of the measured fields (*i.e.,* 3D shape or 3D displacement) and ensures direct links with current CAD and isogeometric softwares [26].

Beaubier et al. [22] and Dufour et al. [23] modeled the studied surface with NURBS patches and, after calibration, deformed the surface by iteratively optimizing the position of the control points to minimize the global residuals. The minimization problem includes an extremely small number of unknowns, but cannot represent surfaces having low order continuities (*i.e.,* parts with groove or machining defect). Dubreuil et al. [24] extended the previous approach to finite element meshes by deforming the surface along the local normal vector. Further, regularization strategies were proposed either by penalizing the Hessian of the minimization scheme [23] or by adding mechanical constrains [25].

The FE-based techniques offer less regular descriptions than standard NURBS models, thereby allowing potentially more complex surfaces to be represented. Further, it is no longer limited to defects that are of C^1 class. However, the large number of degrees of freedom of the optimization problem may lead to poor conditioning, and it is also necessary to start with a good initial guess to obtain consistent results. Thus, global approaches seem more appropriate to study the shape defects of workpieces as the obtained data require few or even no post-processing step compared to point clouds obtained with local approaches. However, it remains necessary to find a compromise between a good description of the surface and a limited number of unknowns for shape measurement via stereocorrelation. The present paper introduces a measurement method for expressing data directly in a predefined library. This system will rely on global stereocorrelation. Unlike previous works [27, 24, 25], the surface will be deformed using displacement fields that represent global (and no longer local) defects. Very recently, Jailin [28] proved that it was possible to determine the amplitude of 8 vibrational modes using global DIC.

The paper is organized as follows. First, the method principle is presented by mainly detailing the writing of the deformation of the surface of interest to match the nominal model with the actual geometry. Second, this measurement method is applied to analyze a medium-sized test piece, and the corresponding measurement protocol is introduced. Third, more detailed analyses of the results in terms of repeatability and sensitivity are discussed.

2. Shape measurements

In this work, the shape defects of a mechanical part will be assessed by global stereocorrelation. Two images of the patterned surface and the nominal CAD model of the part are needed. The registration

technique used herein is divided into two steps [22, 24], namely, i) the self-calibration of the stereo-setup and ii) the deformation of the nominal FE model.

2.1. Self-calibration

Although it is possible to extract information from a scene using uncalibrated cameras [29], calibration is an essential step as soon as metric information is needed [30, 17]. For stereoscopic systems, the calibration consists in determining the relationship between 3D points of the scene and 2D points in the image plane of each camera by determining the different components of the projection matrix $[\mathbf{P}]$ and possibly some distortion parameters.

Different calibration techniques exist and can be classified according to various criteria [31] (*e.g.,* when the approach is explicit [32, 33, 34] or implicit [35]). In the first case, the so-called intrinsic and extrinsic parameters are determined. They allow for the construction of the projection matrices between the 3D world frame and the image frames. In the second case, the different components of the projection matrices are directly optimized. Although the latter approach allows for the measurement of 3D shapes, it does not enable the physical parameters of the cameras to be evaluated. Whichever approach is selected, a pattern is usually applied and at least one pair of images is acquired. At this step, there is still no link between the digital model of the measured part and the measurement data. A registration operation is therefore necessary to study the defects of the measured part.

In the DIC field, another possibility exists, which consists in using the observed part as the calibration target [30]. To perform this self-calibration step, the mathematical description of the studied surface is needed. This model may be based on NURBS descriptions [22, 23] or meshes [24, 25]. The left and right projection matrices ($[\mathbf{P}^l]$, $[\mathbf{P}^r]$) are then determined via global registrations using the nominal description of the surface. The underlying minimization principle is based on the gray level conservation in the images f^l, f^r acquired by the left and right cameras. For a 3D point X_0 in the model frame, let $\mathbf{x}^l$ and $\mathbf{x}^r$ denote its projection on each image plane, the gray level conservation reads

$$f^l(\mathbf{x}^l) = f^r(\mathbf{x}^r) \tag{1}$$

For the studied area in the images, also called region of interest (ROI), an overall minimization is performed to determine the projection matrices

$$([\mathbf{P}^l], [\mathbf{P}^r]) = \underset{[\mathbf{p}^l],[\mathbf{p}^r]}{\mathrm{argmin}} \sum_{ROI} \left(f^l\big(\mathbf{x}^l(\mathbf{X}_0, [\mathbf{p}^l])\big) - f^r\big(\mathbf{x}^r(\mathbf{X}_0, [\mathbf{p}^r])\big) \right)^2 \tag{2}$$

At the end of this self-calibration step, two camera planes are therefore positioned in the CAD or FE coordinate system.

4

2.2. Shape correction using modal databases

Once the components of the projection matrices $[\mathbf{P}^l]$ and $[\mathbf{P}^r]$ are known, the nominal surface will be deformed so as to minimize the correlation residuals. In the approach proposed herein, the deformation of the surface is performed using a defect database obtained by modal analysis, thereby allowing a limited number of unknowns to be used and a simplified post-processing step to be implemented. Let Λ_i denote the amplitude associated with the mode $\mathbf{q}_i$, and $\mathbf{X}_0$ the vector position in the frame of nominal surface points

$$\mathbf{X} = \mathbf{X}_0 + \sum_{i=1}^{N} \Lambda_i \mathbf{q}_i \tag{3}$$

where $\mathbf{X}$ is the estimate of the modal deformation. Analogously to the calibration step, the modal amplitudes Λ_i are determined so as to minimize the global residual over the entire ROI

$$\{\mathbf{\Lambda}\} = \operatorname*{argmin}_{\{\boldsymbol{\lambda}\}} \sum_{ROI} \left(f^l\big(\mathbf{x}^l(\mathbf{X}_0, \{\boldsymbol{\lambda}\})\big) - f^r\big(\mathbf{x}^r(\mathbf{X}_0, \{\boldsymbol{\lambda}\})\big) \right)^2 \tag{4}$$

where $\{\mathbf{\Lambda}\}$ is the column vector that gathers all unknown amplitudes Λ_i.

In a similar way to DIC approaches [17, 36], a Gauss-Newton scheme is used to perform the previous minimizations. It follows that linear systems are solved

$$[\mathbf{H}^q] \, \{\delta\mathbf{\Lambda}\} = \{\mathbf{b}^q\} \tag{5}$$

where $[\mathbf{H}^q]$ and $\{\mathbf{b}^q\}$ denote the "modal" Hessian and residual vector, respectively, and $\{\delta\mathbf{\Lambda}\}$ the corrections to the current estimates of the modal amplitudes. With $[\mathbf{Q}]$ the modal matrix gathering the nodal displacements of unitary modes, the modal Hessian is related to the Hessian $[\mathbf{H}]$ associated with the FE discretization of the nominal shape by

$$[\mathbf{H}^q] = [\mathbf{Q}]^\top \, [\mathbf{H}] \, [\mathbf{Q}] \tag{6}$$

This iterative process is performed until the corrections $\{\delta\mathbf{\Lambda}\}$ become low enough (*i.e.,* $\|\{\delta\mathbf{\Lambda}\}\|_\infty < \epsilon$). In such minimization schemes, the Hessian plays a central role. A sensitivity analysis will be performed in Section 4 to study this matrix on a test case to determine what is the method sensitivity with respect to different parameters.

3. Case study

The previous analysis is applicable to any size of the studied surface, provided the optical system is adequate, and delivers the shape defect in a very compact way (*i.e.,* only few modal amplitudes). Thus, it is desirable to apply this method to large scale parts for which the determination of shape deviations may be data- and computation-intensive. However, in order to validate the method and to compare it with other industrial measuring methods, it is applied to a medium-size part.

3.1. Experimental configuration

The digital model of the studied part, which consists of four Bézier patches connected in curvature, was obtained with CATIA software[1]. The workpiece is 290 mm long along two directions, and its height varies between $+10$ mm and -10 mm compared to the average plane (parallel to the base). In the proposed method, the nominal description of the part is given as a triangular (T3) mesh. To avoid edge effects when searching for the projection matrices $[\mathbf{P}^l]$ and $[\mathbf{P}^r]$, the surface was trimmed leaving a 10-mm strip out of the surface (Figure 1(a)). The piece was then discretized and exported as a T3 mesh with an edge size of 3 mm (Figure 1(b)).
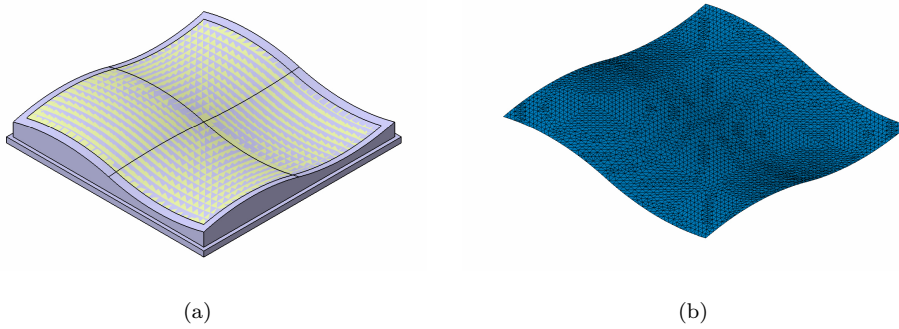

(a)   (b)

Figure 1: Trimmed surface (a) and associated mesh (b)

The choice of the modal basis has an influence on the convergence of the algorithm (*i.e.,* the Hessian $[\mathbf{H}^q]$ depends on the modal basis, see Equation (6)). To study the influence of the selected basis on the Hessian $[\mathbf{H}^q]$, two sets of displacement fields are considered. They are associated with the free vibrational modes obtained with the CAD software Catia. The first basis is directly built as provided by the modal analysis of the software. The second one is constructed by projecting the first basis according to the local surface normal. This second basis is built in order to account for displacements only induced only by shape defects with no motion induced by dimensional defects

$$\text{Basis \#1:} \quad \mathbf{q}_i \qquad\qquad \text{Basis \#2:} \quad (\mathbf{q}_i \cdot \mathbf{n})\,\mathbf{n}$$

where $\mathbf{n}$ denotes the outward unitary normal to any point of the surface of interest, and $\mathbf{q}_i$ the i-th unitary mode. These two bases are then normalized in amplitude so that the maximum displacement is unitary (allowing for a simpler reading of modal amplitudes). As an example, three different modes from the projected basis are shown in Figure 2.

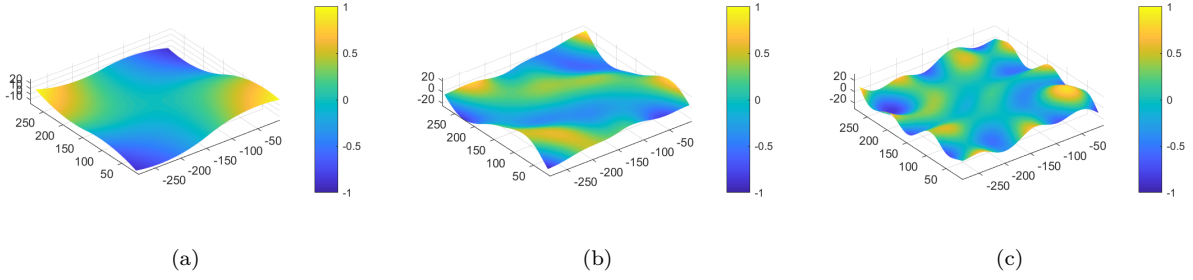[1]https://www.3ds.com/products-services/catia/

Figure 2: Examples of unitary modes from the projected basis: 7-th mode (a), 30-th mode (b), and 49-th mode (c)

The physical part was machined in a parallelepiped made of polyurethane resin using a 3-axis machining center. Since the part had a low stiffness, the clamping forces during the machining operation caused relatively large permanent deformations. The hardware parameters of the optical setup are reported in Table 1.

Table 1: DIC hardware parameters

Cameras	CANON EOS 7D
Definition	5184×3456 pixels (color images)
Color filter	Bayer
Gray Levels rendering	14 bits
Lens	CANON EF 20 mm
Aperture	$f/2.8$
Field of view	530×400 mm^2
Image scale	100 µm/pixel
Stereo-angle	50°
Stand-off distance	600 mm
Image acquisition rate	1-2 fps
Patterning technique	projected pattern (see Figure 3(a) and text)
Pattern feature sizes	3 pixels (projector), 0.5-0.8 mm (on workpiece), 5-8 pixels (cameras)

As the material was not naturally contrasted, a speckle pattern was projected onto the surface. In the present case, a Sony SXRD 4k projector was utilized to project the pattern (Figure 3(a)). The projected random speckle pattern was generated from an image of definition 4096×2160 pixels with a white / black ratio of 60 %. The mean speckle radius of the projected pattern was about 0.4 mm on the workpiece, which induced speckles 8 pixels in diameter on the acquired images (Figure 3(b)). The use of a projector to pattern the surface allowed for an easy study of the influence of the speckle on the registrations. The distortions of the optical setup were estimated based on the 5-parameter model of Brown [37] using the *Camera Calibration* toolbox provided by Matlab R2017b version. The displacements induced by distortions

were less than 25 pixels for the region of interest.

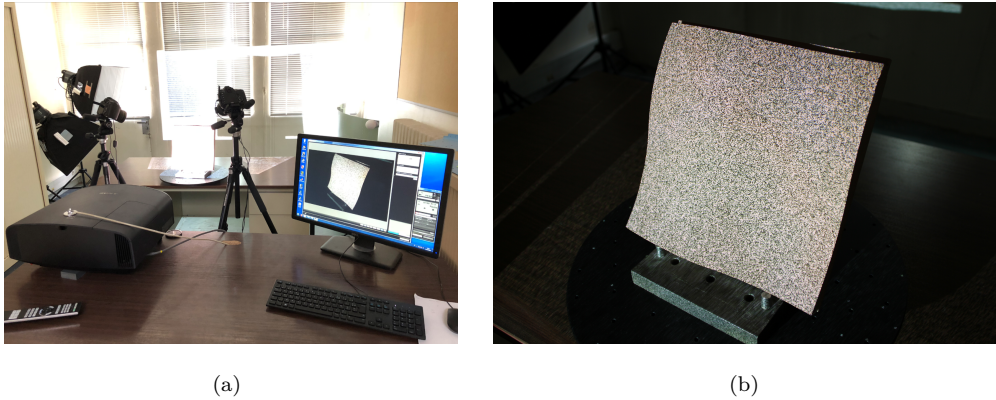(a)   (b)

Figure 3: Stereoscopic system (a) and pattern projected onto the workpiece surface (b)

Five images were acquired with each camera under the same experimental conditions in order to estimate the acquisition noise. Considering the region of interest in the images, and subtracting the images (of the same camera), the gray level fluctuations associated with each pixel are obtained. Figure 4 shows the gray level fluctuations for the left and the right devices. It is worth noting that the dynamic ranges of both series of images are equal to 255 gray levels.
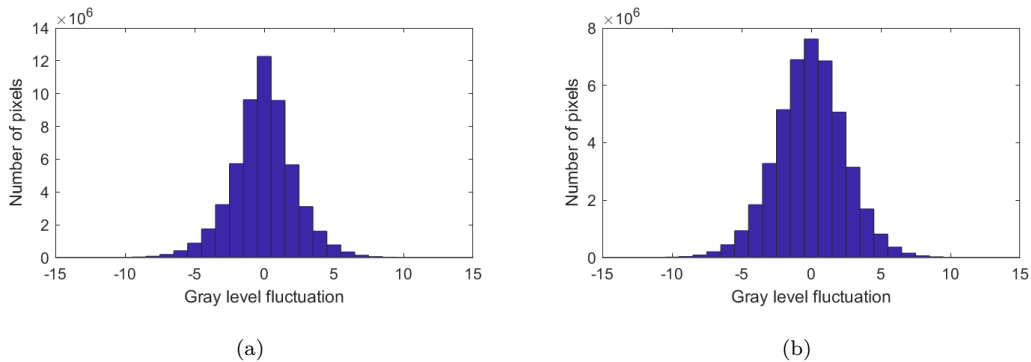

(a)   (b)

Figure 4: Gray level fluctuation for left (a) and right (b) cameras

For both devices, the noise is Gaussian with a very small mean; the standard deviations are equal to 3.4 and 2.5 gray level, respectively. This value can be used to determine the measurement uncertainty for any given configuration [38, 39].

3.2. Reference measurement

In order to validate the consistency of the results obtained with the proposed method, they were compared with the measurements obtained with a reference system. Currently, structured light scanning devices appear to be one of the most efficient optical systems to measure parts with complex shapes [40]. In the present work,

a fringe projection system ATOS Core 300 SN: 171215 was used. The system consisted of two cameras (focal length: 12.5 mm) and a projector (focal length: 8.0 mm), allowing a volume of about $300 \times 230 \times 230$ mm^3 to be investigated. According to the manufacturer datasheet, the standard deviation of shape error obtained with this system is 3 µm.

After measuring the workpiece using the ATOS Core system, a cloud of about 5.9 million points was obtained. In order to validate the method and compare it to this reference system, it is essential to estimate the shape defect of the part. A non-rigid registration algorithm [41] was used by considering $K = 10$ neighbors sorted in a cylinder of radius $R = 4$ mm and height $h = 10$ mm. The shape defect of the part was estimated with $N = 50$ modes in both bases. The application of the non-rigid registration made it possible to obtain the shape defect of the part and also the associated residual (related to acquisition noise, and the completeness of the considered basis). The shape defect can be represented either by a bar diagram to give the values of modal amplitudes (Figure 5(a-b)) or by displacement maps (Figure 5(c-d)). The two maps associated with the shape corrections are very close, with a root mean square (RMS) difference of 26 µm, and the modal amplitudes are very similar too.
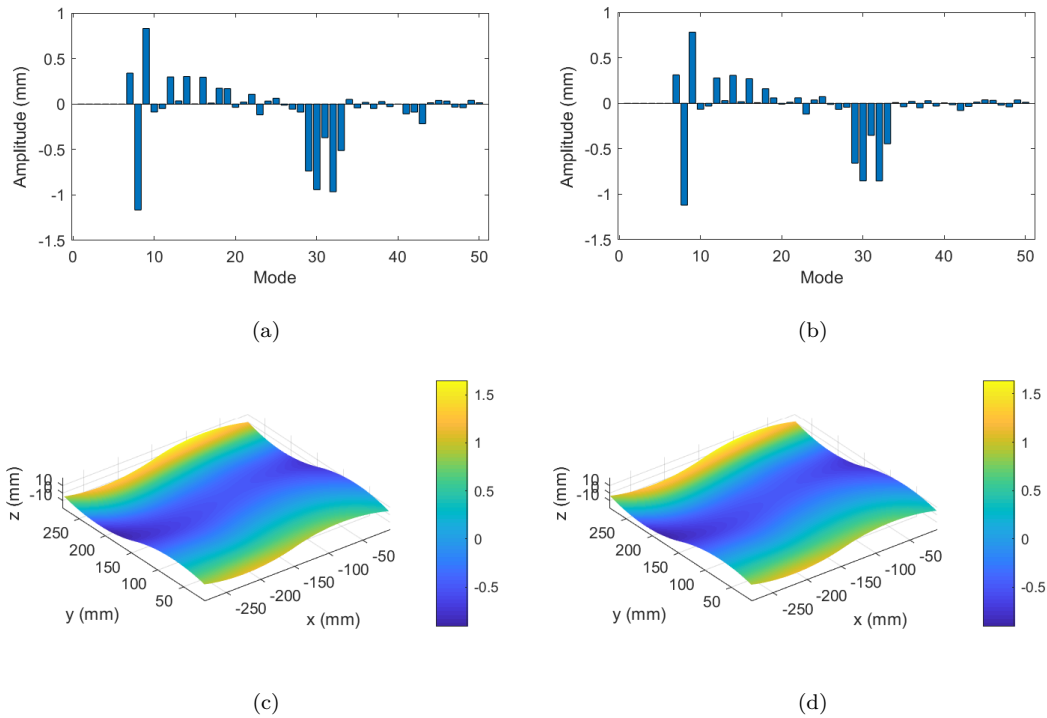

Figure 5: (a-b) Modal amplitudes (expressed in mm) using ATOS Core point cloud with the two modal bases. (c-d) Corresponding shape defects (expressed in mm)

The residuals are also reported in both ways. It is worth noting that rigid body motions, *i.e.,* the first 6 modes, are not displayed. Figure 6 highlights the shape offsets projected according to the local norm

between the deformed nominal part and the point cloud. For any basis, the results are very close (RMS residual of 7.6 µm for both bases). In the present case, the residuals associated with either basis do not allow their relevance to be discriminated. However, the shape residuals between the nominal geometry and the measurement are low enough to state that both bases are able to describe the studied shape defects.
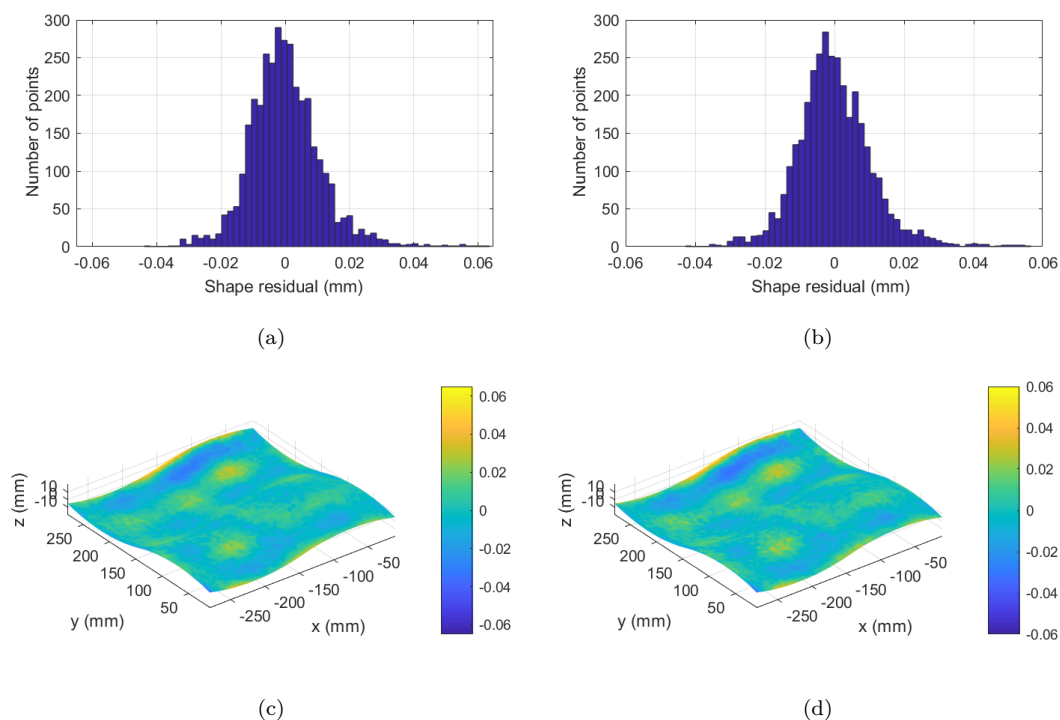

(a)

(b)

(c)

(d)

Figure 6: (a-b) Histograms of deviation between ATOS Core point cloud and estimated shape based on the two modal bases. (c-d) Corresponding deviation maps (expressed in mm)

3.3. Modal stereocorrelation results

In the following analyses (Table 2), a first set of results is reported for modal stereocorrelation. To follow the proposition of Dubreuil et al. [24], the second modal basis was selected (the other one will be studied in Section 4 for comparison purposes).

Table 2: DIC analysis parameters

DIC software	Correli 3.0 [42]
Image filtering	None
Element size	3 mm
Shape functions	Linear
Evaluation points (per element)	28
Modal bases	44 modes (see text)
Matching criterion	Quadratic differences
Interpolant	Linear
Shape noise-floor	see text

The pair of images used for the registration is shown in Figure 7. The self-calibration step can be performed either with the nominal model of the part of interest or with its actual dimensions [22]. If available, the latter information is more desirable and allows for faster convergence. In the present case, the self-calibration was performed using the ATOS Core data, focusing this analysis on the shape defect determination only. This will leave the calibration step out of the discussion. Modal stereocorrelation was performed with the first 44 modes for the shape defect basis, that is to say modes 7 to 50 (*i.e.,* the rigid body motions were not considered).

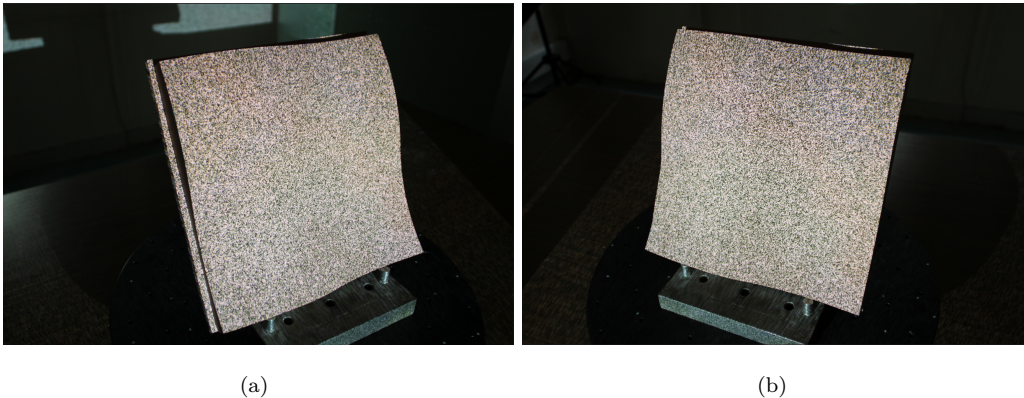(a)   (b)

Figure 7: Left (a) and right (b) acquired pictures for the first set of analyses via modal stereocorrelation

The correlation residual map provides the relevant information on the optimization results. A low and uniform residual all over the ROI indicates that the registration was successful and the selected modal basis was complete enough to correctly describe the shape defects [23]. Heterogeneities in the residual map may indicate a mismatch of the actual solution and the optimal one due to the incompleteness of the selected basis or bad optimization solution. The residuals maps before and after shape correction are reported in Figure 8. Before shape corrections, the residual map is heterogeneous almost everywhere. Conversely, at the

end of the shape correction, the residuals are lower (*i.e.,* they decreased from 5.2 % of the dynamic range to 1.5 %), which validates the registration. It can be noted that some higher levels are observed close to the top right corner, which indicates that in this area the shape corrections were not totally satisfactory. These correlation residuals are higher than the acquisition noise (Figure 4), which may indicate a local mismatch of the shape in that area.
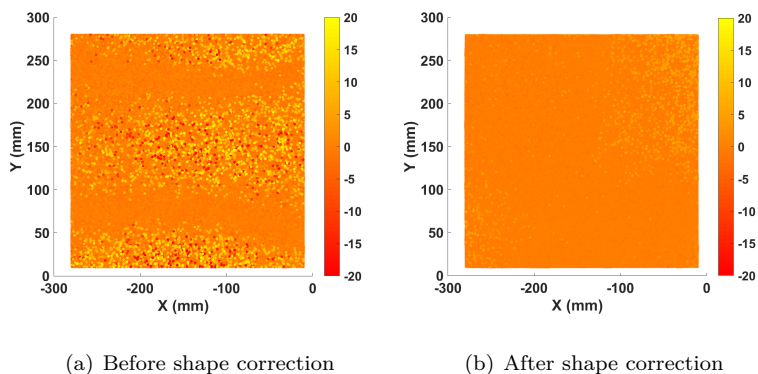

(a) Before shape correction   (b) After shape correction

Figure 8: Correlation residual maps (expressed in % of dynamic range) before and after shape corrections

The shape corrections are reported in Figure 9(a-b). Qualitatively, they are close to those obtained with the reference method (Figure 5(b-d)). Quantitatively, the map of shape differences along the surface normal is shown in Figure 9(c) and the corresponding histogram in Figure 9(d). The range of differences is less than ±80 µm and the corresponding standard deviation is equal to 18 µm. These results validate the modal stereocorrelation method. It is worth noting that one of the corners where the shape residual is high is also the one where the correlation residual is high.

12

(a) Shape defect map

(b) Modal amplitudes

(c) Difference map
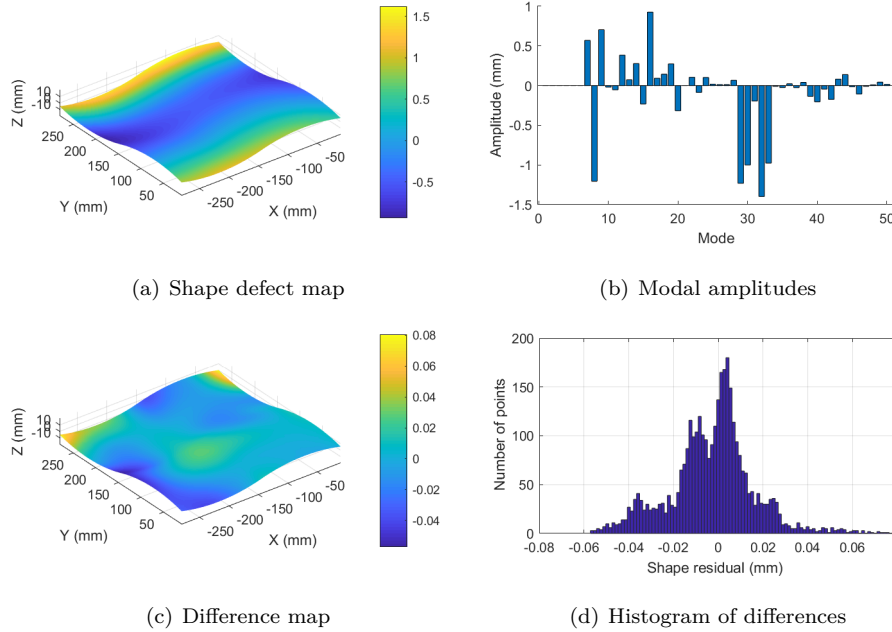
(d) Histogram of differences

Figure 9: Results with modal stereocorrelation (a,b), and comparison with ATOS Core results (c,d). The unit of the color bars is mm

The acquisition and data processing time of both ATOS Core system and the purposed DIC method are similar for the studied surface, respectively 14 and 17 minutes. However, on large scale surfaces, this time will remain identical for DIC and may be decreased by optimizing the matlab code, whereas it will greatly increase for the ATOS Core system. The next question to address is whether such results are repeatable for a given configuration, but also for different configurations. The answer is provided by performing a sensitivity analysis.

4. Sensitivity analysis

In this section, a sensitivity analysis is performed to various parameters that can be set by the user. Since Equation (5) is solved iteratively, it is important to ensure that the Hessian $[\mathbf{H}^q]$ is properly conditioned. The corresponding eigenvalues can be used to optimize tests with respect to their sensitivities to acquisition noise [43]. This matrix mainly depends on three parameters [22, 26]:

- $\boldsymbol{\nabla} f^l$ and $\boldsymbol{\nabla} f^r$, corresponding to the gray-level contrasts and therefore depending among other things on the projected speckle. The modification of the speckle pattern is delicate when obtained by spraying black and white paints. It is a lot easier to investigate when it is projected (as herein);

- $\frac{\partial \mathbf{x}^l}{\partial \mathbf{X}}$ and $\frac{\partial \mathbf{x}^r}{\partial \mathbf{X}}$ characterize the pixel shifts induced by 3D offsets. These partial derivatives are directly related to the projection matrices $[\mathbf{P}^l]$ and $[\mathbf{P}^r]$ relating the homogeneous coordinates in each camera

plane to those of the considered physical point. These matrices depend on the intrinsic and extrinsic parameters of each camera [34, 17];

- and in the present case the modal matrix [**Q**], which depends on the selected modal basis.

4.1. Influence of modal basis and speckle size

The relevance of the two bases introduced previously is now discussed. As shown in Section 3.2, the two bases led to essentially the same result when using the ATOS Core system. They made it possible to represent shape defects with an RMS residual less than 7.6 µm (see Figure 6). To study the influence of the modal basis on the defect shape identification, the global correlation residual, which is the RMS of the gray level differences normalized by the dynamic range of reference pictures (*i.e.,* 255 gray levels), is studied. Figure 10 shows the change of the global correlation residual during the shape correction phase using the two modal bases. Figure 10(a) corresponds to a coarse speckle (mean speckle diameter $\approx$ 0.8 mm or approximately 8 pixels). The results of Figure 10(b) are obtained with a fine speckle (mean speckle diameter $\approx$ 0.5 mm or approximately 5 pixels).
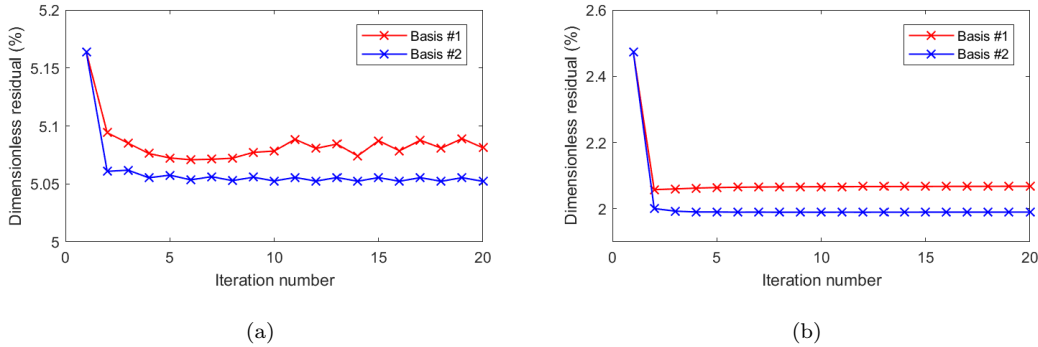

Figure 10: Correlation residuals during shape corrections with the two modal bases for coarse (a) and fine (b) speckles

In Figure 10(a), the first basis leads to oscillations with a gradual divergence in the last iterations, while for the second basis, convergence is achieved in a regular way. The second basis makes it easier for the registration to converge, which can be explained by the regularizing effect of the projection of displacements according to the local surface normal [24]. Moreover, when the registration converges for both bases, the correlation residuals are slightly lower with the second one (Figure 10(b)). Based on these two observations, the second basis is the most relevant and will be kept for future investigations.

In the present case, finer speckles led to lower residuals when compared to the coarser ones, which was already observed in other situations [44, 45]. In the studied case, the best results are obtained with speckle diameters of 5 pixels, in line with the recommendations of the International Digital Image Correlation Society (*i.e.,* speckle size of 3-5 pixels [45]).

The influence of the camera position on the correlation results is investigated in the sequel. To perform this analysis, three camera positions were chosen near the initially selected stereoscopic configuration (Figure 11). The results presented in Section 3 were obtained using configuration #3. For these four configurations, five images were acquired with each camera to study the repeatability of the results. The projected speckle was identical in all four configurations, and the position and orientation of the workpiece relative to the projector did not change.
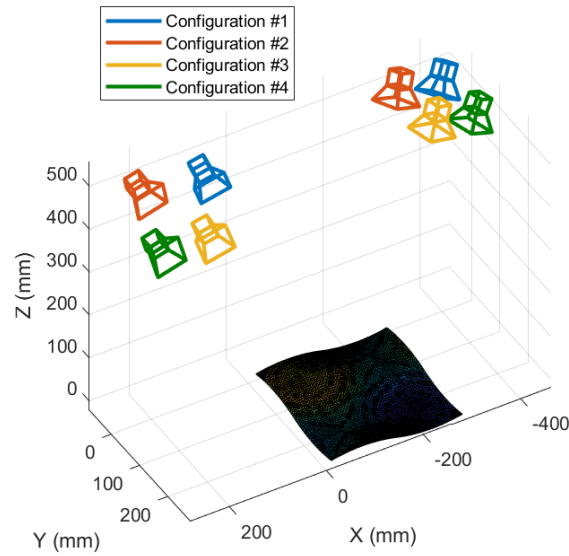
Figure 11: Investigated camera configurations

To perform the calculations, the first 44 shape defect modes of the second basis were used (*i.e.,* modes 7 to 50, the first 6 are rigid body modes). Since there are 5 left images and 5 right images, 25 pairs of images can be analyzed (Left1-Right1, Left1-Right2, etc.), allowing an average result to be constructed and the fluctuations to be analyzed. The following results correspond to the mean results computed from the 25 image pairs for each configuration. The average shape correction maps for each configuration (Figure 12) all appear essentially identical and very close to the reference case (Figure 9(a)).

(a) Configuration #1

(b) Configuration #2
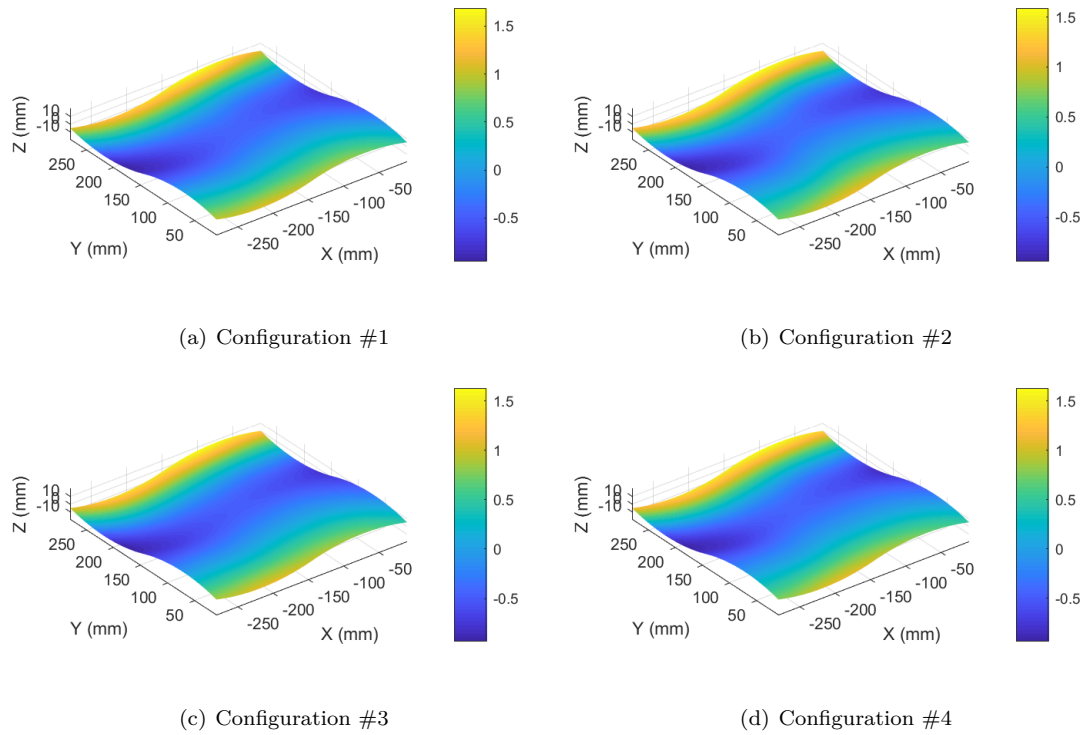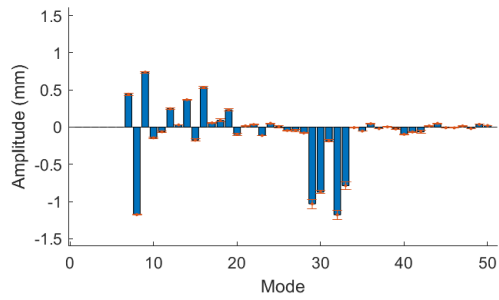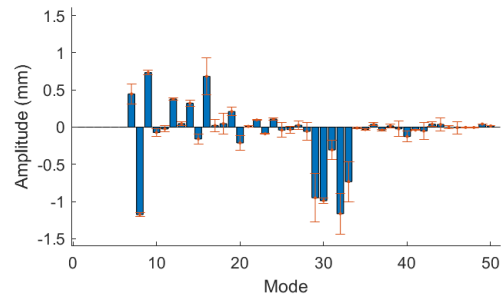
(c) Configuration #3

(d) Configuration #4

Figure 12: Average correction map (expressed in mm) for the four studied configurations (Figure 11)

For the 25 pairs of images, the mean value and the standard deviation on each modal amplitude were computed and are reported in Figure 13. Regarding the modal amplitudes, although the distribution is generally similar and close to the reference case (Figure 9(b)), some minor changes are observed. It is worth noting that the error bars differ from one configuration to another.
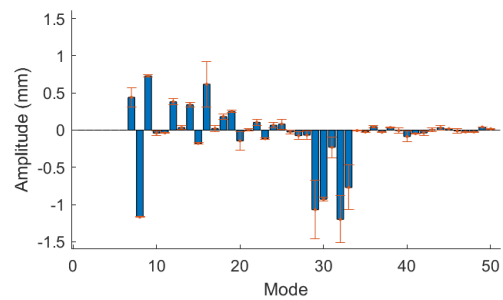
(a) Configuration #1   (b) Configuration #2
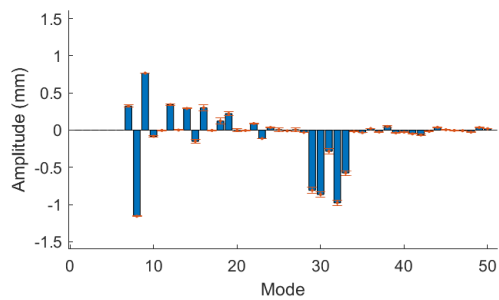
(c) Configuration #3   (d) Configuration #4

Figure 13: Average modal amplitudes for the four studied configurations (Figure 11) and corresponding standard deviations (error bars)

By using the mean value of the modal amplitudes (Figure 13), the associated shape defect map in each configuration are compared to the reference measurement (*i.e.,* with the ATOS Core system). Figure 14 shows that the global shape defect is close to ± 15 µm from the reference measurement with a root mean square difference varying between 53 µm and 18 µm depending on the studied configuration. Thus, the relative position of the cameras has a significant impact on the shape defect determination.

(a) Configuration #1, STD: 33 µm

(b) Configuration #2, STD: 53 µm

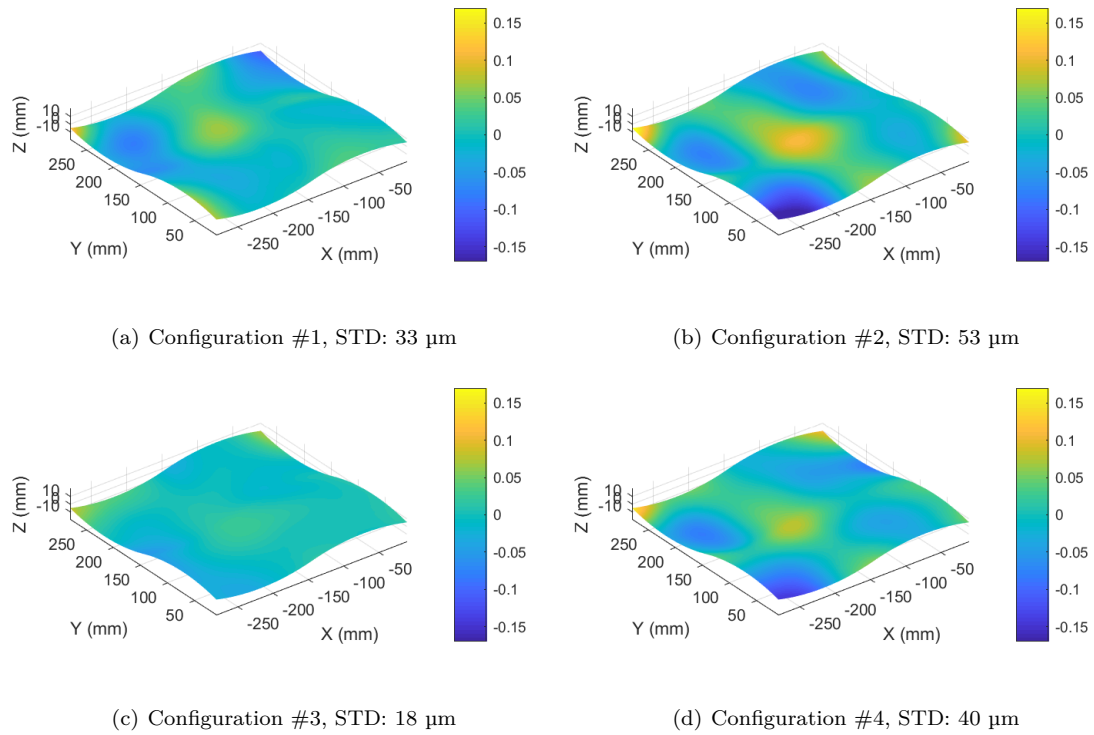(c) Configuration #3, STD: 18 µm

(d) Configuration #4, STD: 40 µm

Figure 14: Average map of differences (expressed in mm) between modal stereocorrelation and ATOS measurements

Figure 13 also highlights two configurations for which the modal amplitude uncertainty is higher than the other ones. By looking more specifically at the results, one can distinguish two different series of modal amplitudes that give approximately the same correction map (see Figure 15). This observation explains the large error bar on the modal amplitude.
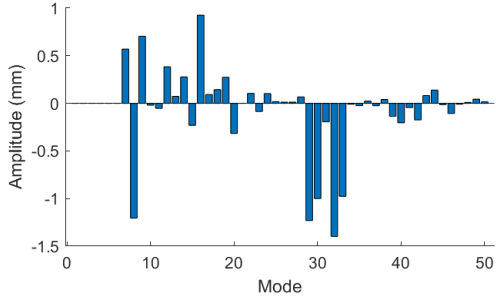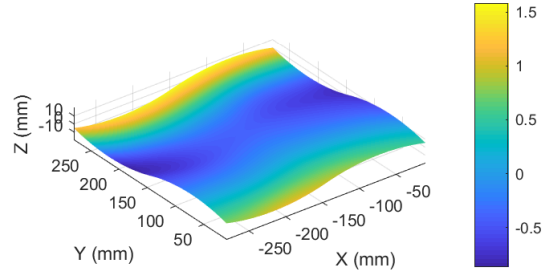
(a) Solution 1
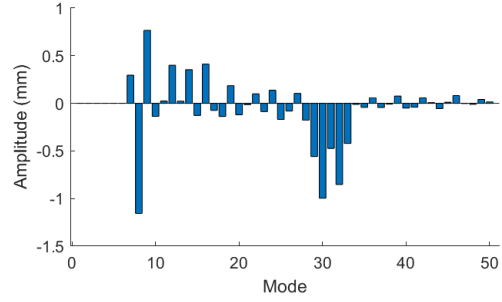
(b) Solution 2
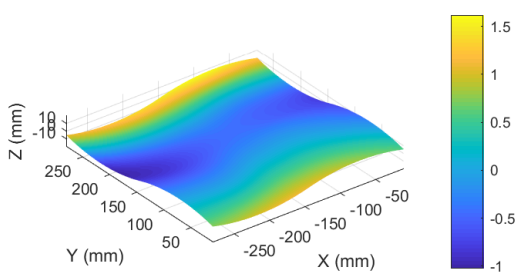
(c) Solution 1

(d) Solution 2

Figure 15: Pair of solutions for configuration #2. The unit of the color bars is mm

The error bars applied to the modal amplitudes Λ_i do not make it possible to visually obtain an indication of the repeatability of the shape defect itself. This is why one should look at the standard deviation not in terms of modal amplitudes, but in terms of displacements along the local surface normal. Figure 16 reports the standard deviation of the shape defect. The shape defect uncertainty varies according to the chosen configuration. The mean standard deviation ranges between 17 µm (configuration #1) and 120 µm (configuration #2). This result confirms the fact that the measurement configuration (and thus the corresponding projection matrices $[\mathbf{P}^l]$ and $[\mathbf{P}^r]$) has an important influence. Such result also calls for an optimization of the stereo-vision system.
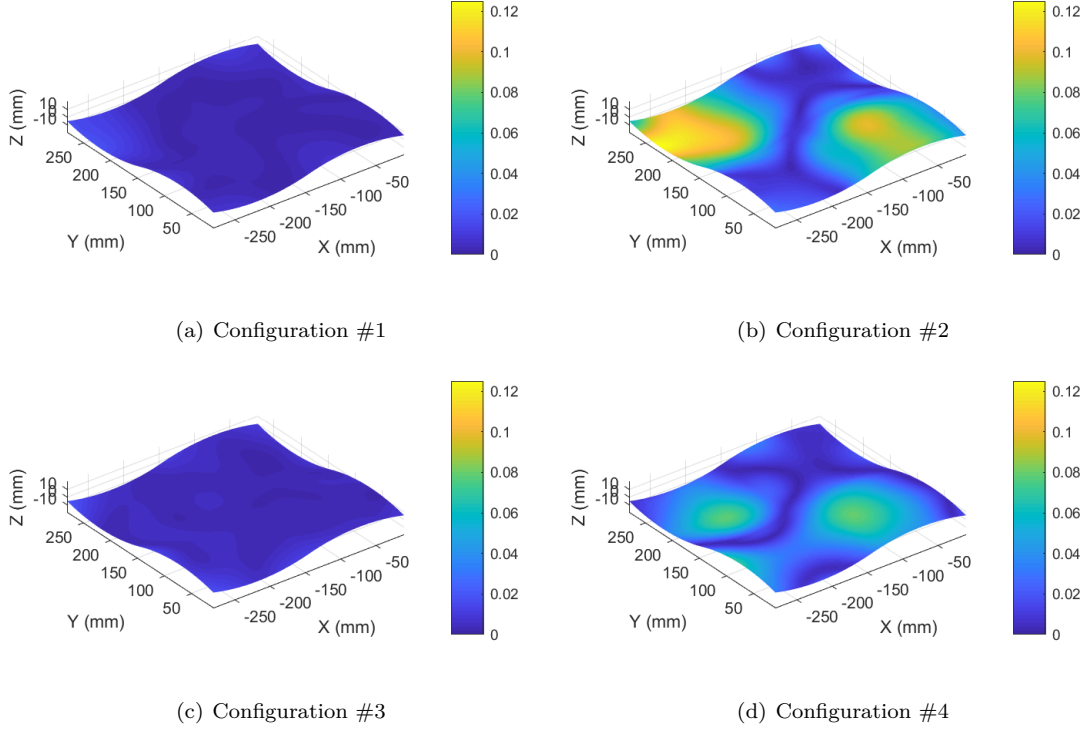
19

(a) Configuration #1

(b) Configuration #2

(c) Configuration #3

(d) Configuration #4

Figure 16: Standard deviation map (expressed in mm) of the shape defect

4.3. Influential shape defects

For the different measurement configurations, one can study the Hessian matrix $[\mathbf{H}^q]$. To study the ability of the method to detect some defects in a given measurement configuration, it is necessary to analyze the eigenvalues of the Hessian [43]. A high eigenvalue defines an eigenmode that is very sensitive, *i.e.,* its uncertainty is very low. Conversely, a low eigenvalue will be more impacted by image noise.

A spectrum analysis of the Hessians makes it possible to determine the influence of the measurement configuration on the detection of some defects. Figure 17 shows the spectra associated with measurement configurations #1 to #4. It is observed the spectrum slightly varies from one configuration to another but the general tendency remains the same. In all studied configurations, 12 modes are much less influential than the other 32. It is worth noting that, based on the trends of these spectra, if the considered basis contained too many modes, the conditioning would further degrade and may lead to numerical instabilities.
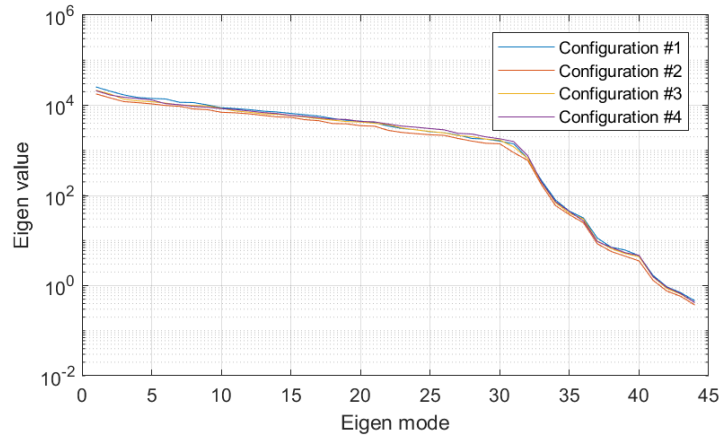
Figure 17: Spectra of Hessians for the four studied configurations (Figure 11)

It will be shown hereafter that these less influential modes have high spatial frequencies, whereas the most influential ones have low spatial frequencies. It is worth noting that, based on these spectra, another analysis could be performed using less eigenmodes to ensure a good conditioning of the problem while keeping a good representativeness of the studied shape defect. This study is not presented herein as the conditioning was not problematic in the presented study. For each configuration, one can study the displacement map associated with the most sensitive eigenmode. Figure 18 shows the displacement maps associated with the most influential mode (eigenvector #1 referring to the above spectra, see Figure 17). The edges of the mesh were intentionally left out to better perceive the shape variations. The most influential eigenmode is not the same depending on the selected measurement configuration. However, all of them have rather high wavelengths.

(a) Configuration #1

(b) Configuration #2

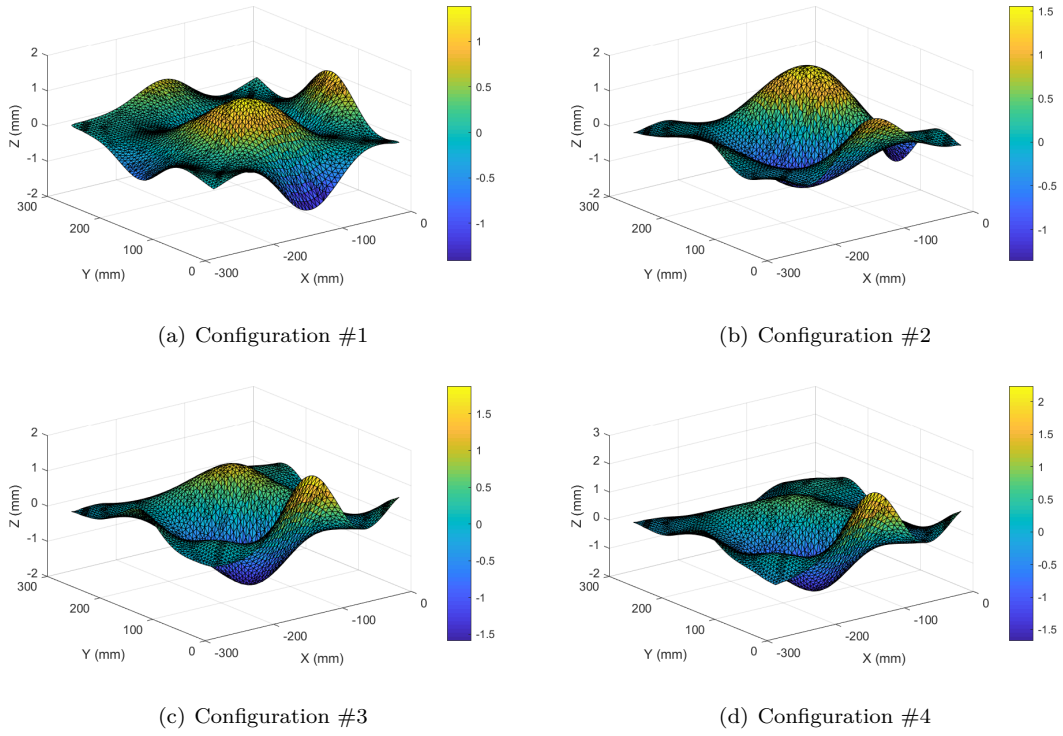(c) Configuration #3

(d) Configuration #4

Figure 18: Most sensitive eigenmodes (*i.e.,* eigenvector #1)

Figure 19 reports the least influential eigenmode, which is different for the four configurations. Their fluctuations have significantly larger spatial frequencies than the most sensitive mode (Figure 18).
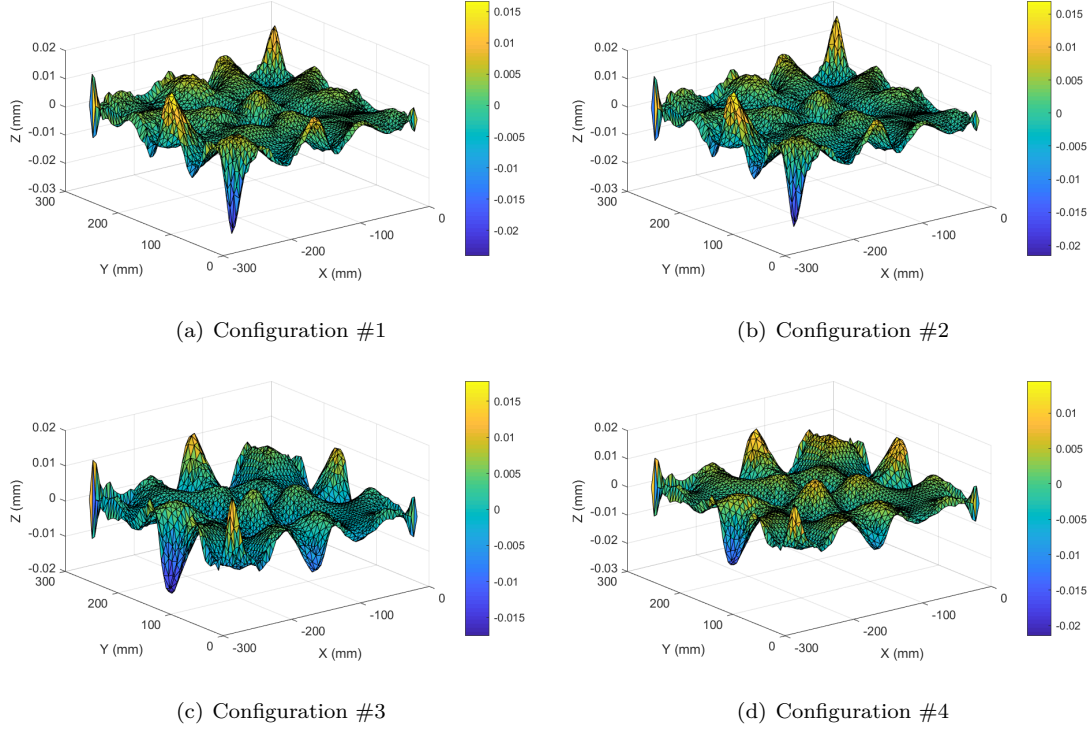
(a) Configuration #1

(b) Configuration #2

(c) Configuration #3

(d) Configuration #4

Figure 19: Least influential eigenmodes (*i.e.,* eigenvector #44)

Thus, according to Figures 17, 18 and 19, the high frequency defects will be naturally filtered by modal stereocorrelation while the low frequency ones will be captured. However, if one is interested in detecting local defects (which require the use of high frequency representations), one may turn to the residual map (Figure 8) to locate the areas in which the computed shape mismatch with the real surface should be enriched.

4.4. Discussion

In this section, a detailed analysis on the effect of different parameters on the stereocorrelation results is presented. Several parameters have a significant influence:

- **Modal basis**: two modal bases were studied. Although the shape defect could be represented by either one, Figure 10 shows that the choice of the basis had a first order influence on the defect determination. Further, the projected basis has a regularizing effect for any of the speckle patterns. In this study, both bases were built from discrete modal decomposition (DMD) elements. This technique enable any types of surface to be analyzed but constrains the shape defects to be continuous. However, if one is interested in detecting discontinuous defects, it is possible to locate them based on residual map, and then enrich the basis.

23

- **System configuration**: the relative position and orientation of the cameras with respect to the workpiece had an influence on several parameters of the method:

  - If the industrial measurement system (ATOS Core) is assumed to be the reference, the difference between the correlation results and those obtained with ATOS Core characterize the accuracy of modal stereocorrelation. Thus, according to Figure 14, the average shape defect is close with respect to the reference solution with an RMS difference ranging between 18 µm and 53 µm depending on the stereovision configuration.

  - The computed shape defect repeatability is also impacted by the camera configuration. In some cases, the shape defect estimates are highly repeatable (standard deviation less than 22 µm) whereas in some cases it reached 125 µm (Figure 16). However, the computed shape defects are similar and close to the reference measurement (with an RMS difference ranging from 18 µm to 53 µm as shown in Figure 14).

  - The defect sensitivity depends on the camera configuration too (Figures 18 and 19). It is also worth noting that the low spatial frequency defects are generally the most influential, which means the proposed method will easily detect the first eigenmodes. If one is interested in looking for local defects, a residual map analysis highlights the area(s) of the surface where a local defect may be present so that a multiscale analysis could be performed around this location or an enrichment strategy could be followed.

5. Conclusion and Outlook

In this work, modal stereocorrelation was implemented to measure shape defects. To avoid issues related to the measured data registration with respect to the nominal model, a self-calibration step was performed. The originality of the method lies in the use of modal bases, thereby allowing for dense representations of surface shape defects, while limiting the number of unknowns of the problem (and therefore its solution complexity) and also reducing the post-processing phase.

The developed method was applied to a medium-sized test part ($290 \times 290 \times 20$ mm^3) and the obtained results were compared to the defect found with a reference system (ATOS Core). The shape defects measured with this method were close to those found with the reference system, with standard differences not exceeding 53 µm for an overall shape defect amplitude of approximately 2 mm. These differences can be decreased down to a standard deviation of 18 µm depending on the measurement configuration. To avoid any issues arising from the self-calibration step, and to only study the limits of the shape defect measurement phase, the self-calibration step was carried out using the ATOS Core measurements for the surface of interest.

In future work, the self-calibration step will be optimized. This method will also be applied to larger workpieces. Last, since the uncertainties of the system depend on the positions of the cameras with respect to

the part of interest, the sensitivity analysis can be used to determine the optimal configuration for measuring a known defect database. Last, since video-projected patterns were considered herein, their optimization may also be investigated.

Acknowledgments

References

[1] ISO4287, Geometrical product specifications (gps). surface texture: profile method. terms, definitions and surface texture parameters., 1997.

[2] X. Han, J. Jin, M. J. W. Wang, Guided 3d point cloud filtering, Multimedia Tools and Applications 77 (2018) 17397–17411.

[3] E. Savio, L. De Chiffre, R. Schmitt, Metrology of freeform shaped parts, CIRP annals 56 (2) (2007) 810–835.

[4] R. Schmitt, M. Peterek, E. Morse, W. Knapp, M. Galetto, F. Härtig, G. Goch, B. Hughes, A. Forbes, W. Estler, Advances in large-scale metrology – review and future trends, CIRP Annals 65 (2) (2016) 643–665.

[5] H. Schwenke, U. Neuschaefer-Rube, T. Pfeifer, H. Kunzmann, Optical methods for dimensional metrology in production engineering, CIRP Annals 51 (2) (2002) 685–699.

[6] P. J. Besl, N. D. McKay, Method for registration of 3-d shapes, in: Sensor Fusion IV: Control Paradigms and Data Structures, Vol. 1611, International Society for Optics and Photonics, 1992, pp. 586–607.

[7] L. Zhu, J. Barhak, V. Srivatsan, R. Katz, Efficient registration for precision inspection of free-form surfaces, The International Journal of Advanced Manufacturing Technology 32 (5-6) (2007) 505–515.

[8] N. Senin, B. Colosimo, M. Pacella, Point set augmentation through fitting for enhanced icp registration of point clouds in multisensor coordinate metrology, Robotics and Computer-Integrated Manufacturing 29 (1) (2013) 39–52.

[9] W. Huang, D. Ceglarek, Mode-based decomposition of part form error by discrete-cosine-transform with implementation to assembly and stamping system with compliant parts, CIRP Annals-Manufacturing Technology 51 (1) (2002) 21–26.

[10] F. Zernike, Phase contrast, a new method for the microscopic observation of transparent objects, Physica 9 (7) (1942) 686–698.

[11] S. Ganti, B. Bhushan, Generalized fractal analysis and its applications to engineering surfaces, Wear 180 (1-2) (1995) 17–34.

[12] P. Franciosa, S. Gerbino, S. Patalano, Simulation of variational compliant assemblies with shape errors based on morphing mesh approach, The International Journal of Advanced Manufacturing Technology 53 (1-4) (2011) 47–61.

[13] S. Samper, F. Formosa, Form defects tolerancing by natural modes analysis, Journal of computing and information science in engineering 7 (1) (2007) 44–51.

[14] ISO12181-1:2011, Geometrical product specifications (gps) – roundness – part 1: Vocabulary and parameters of roundness, Standard, International Organization for Standardization (2011).

[15] XP E04-007, Geometrical product specifications (gps) - discrete modal decomposition - analysis method, Standard, Association Française de Normalisation (AFNOR) (2015).

[16] F. Thiébaut, C. Lacroix, L. Andolfatto, C. Lartigue, Evaluation of the shape deviation of non rigid parts from optical measurements, The International Journal of Advanced Manufacturing Technology 88 (5) (2017) 1937–1944.

[17] M. A. Sutton, J. J. Orteu, H. Schreier, Image correlation for shape, motion and deformation measurements: basic concepts, theory and applications, Springer Science & Business Media, 2009.

[18] J.-J. Orteu, F. Bugarin, J. Harvent, L. Robert, V. Velay, Multiple-camera instrumentation of a single point incremental forming process pilot for shape and 3d displacement measurements: methodology and results, Experimental Mechanics 51 (4) (2011) 625–639.

[19] Z. Gao, F. Li, Y. Liu, T. Cheng, Y. Su, Z. Fang, M. Yang, Y. Li, J. Yu, Q. Zhang, Tunnel contour detection during construction based on digital image correlation, Optics and Lasers in Engineering 126 (2020) 105879.

[20] B. Wagne, S. Roux, F. Hild, Spectral approach to displacement evaluation from image analysis, Eur. Phys. J. AP 17 (2002) 247–252.

[21] G. Besnard, F. Hild, S. Roux, "finite-element" displacement fields analysis from digital images: application to portevin–le châtelier bands, Experimental Mechanics 46 (6) (2006) 789–803.

[22] B. Beaubier, J.-E. Dufour, F. Hild, S. Roux, S. Lavernhe, K. Lavernhe-Taillard, Cad-based calibration and shape measurement with stereodic, Experimental Mechanics 54 (3) (2014) 329–341.

[23] J.-E. Dufour, S. Leclercq, J. Schneider, S. Roux, F. Hild, 3d surface measurements with isogeometric stereocorrelation-application to complex shapes, Optics and Lasers in Engineering 87 (2016) 146–155.

[24] L. Dubreuil, J.-E. Dufour, Y. Quinsat, F. Hild, Mesh-based shape measurements with stereocorrelation, Experimental Mechanics 56 (7) (2016) 1231–1242.

[25] J.-E. Pierré, J.-C. Passieux, J.-N. Périé, Finite Element Stereo Digital Image Correlation: Framework and Mechanical Regularization, Experimental Mechanics 57 (3) (2017) p.443–456.

[26] J.-E. Dufour, F. Hild, S. Roux, Shape, Displacement and Mechanical Properties from Isogeometric Multiview Stereocorrelation, J. Strain Analysis 50 (7) (2015) 470–487.

[27] J. Dufour, B. Beaubier, S. Roux, F. Hild, Displacement measurement using CAD-based stereo-correlation with meshes, in: ICEM conference, 2014.

[28] C. Jailin, Full field modal measurement with a single standard camera, Optics and Lasers in Engineering 107 (2018) 265–272.

[29] R. I. Hartley, Euclidean reconstruction from uncalibrated views, in: Joint European-US workshop on applications of invariance in computer vision, Springer, 1993, pp. 235–256.

[30] O. D. Faugeras, Q.-T. Luong, S. J. Maybank, Camera self-calibration: Theory and experiments, in: European conference on computer vision, Springer, 1992, pp. 321–334.

[31] J. Salvi, X. Armangué, J. Batlle, A comparative review of camera calibrating methods with accuracy evaluation, Pattern recognition 35 (7) (2002) 1617–1635.

[32] R. Tsai, A versatile camera calibration technique for high-accuracy 3d machine vision metrology using off-the-shelf tv cameras and lenses, IEEE Journal on Robotics and Automation 3 (4) (1987) 323–344.

[33] J. Weng, P. Cohen, M. Herniou, Camera calibration with distortion models and accuracy evaluation, IEEE Transactions on Pattern Analysis & Machine Intelligence (10) (1992) 965–980.

[34] O. Faugeras, Three-dimensional computer vision: a geometric viewpoint, MIT press, 1993.

[35] E. L. Hall, J. B. Tio, C. A. McPherson, F. A. Sadjadi, Measuring curved surfaces for robot vision, Computer (12) (1982) 42–54.

[36] F. Hild, S. Roux, Digital image correlation, in: P. Rastogi, E. Hack (Eds.), Optical Methods for Solid Mechanics. A Full-Field Approach, Wiley-VCH, Weinheim (Germany), 2012, pp. 183–228.

[37] D. C. Brown, Close-range camera calibration, Photogramm. Eng 37 (8) (1971) 855–866.

[38] ISO, International Vocabulary of Metrology - Basic and General Concepts and Associated Terms (VIM), International Organization for Standardization, Geneva (Switzerland), 2007.

[39] ISO, Guide to the Expression of Uncertainty in Measurements (GUM), International Organization for Standardization, Geneva (Switzerland), 1995.

[40] M. Guerra, F. Lavecchia, G. Maggipinto, L. Galantucci, G. Longo, Measuring techniques suitable for verification and repairing of industrial components: A comparison among optical systems, CIRP Journal of Manufacturing Science and Technology.

[41] F. Thiébaut, S. Bendjebla, Y. Quinsat, C. Lartigue, Nonrigid registration for form defect identification of thin parts, Journal of Computing and Information Science in Engineering 18 (2) (2018) 021012.

[42] H. Leclerc, J. Neggers, F. Mathieu, F. Hild, S. Roux, Correli 3.0, IDDN.FR.001.520008.000.S.P.2015.000.31500, Agence pour la Protection des Programmes, Paris (France) (2015).

[43] M. B. R. Bertin, F. Hild, S. Roux, Optimization of a cruciform specimen geometry for the identification of constitutive parameters based upon full-field measurements, Strain 52 (4) (2016) 307–323.

[44] Y. Su, Q. Zhang, X. Xu, Z. Gao, Quality assessment of speckle patterns for dic by consideration of both systematic errors and random errors, Optics and Lasers in Engineering 86 (2016) 132–142.

[45] International Digital Image Correlation Society, A good practices guide for digital image correlation, http://www.idics.org/guide/ (2018).